Engineering Research Express

PAPER

Emulating atmospheric turbulence effects on a micro-mirror array: assessing the DMD for use with free-space-to-fibre optical connections

David M Benton*, Andrew D Ellis, Yiming Li and Zhouyi Hu

Aston Institute of Photonic Technologies, Aston University, Birmingham, United Kingdom, B4 7ET

* Author to whom any correspondence should be addressed.

E-mail: d.benton@aston.ac.uk

Keywords: micromirror array, atmospheric turbulence, zernike modes, atmospheric emulation

OPEN ACCESS

RECEIVED
25 March 2022

REVISED
9 June 2022

ACCEPTED FOR PUBLICATION
21 June 2022

PUBLISHED
19 October 2022

Abstract

Emulated atmospheric turbulence effects constructed from a set of 22 Zernike modes have been written upon a DMD micromirror array operating as a binary amplitude spatial light modulator. Sequences of aberrated frames with controlled amounts of turbulence have been produced and can be operated at controlled rates that can exceed 1 kHz rates which can be seen in strong turbulence. In this case 400 Hz was chosen and the scintillation levels observed for the same turbulence sequence with single, few and multi-mode fibres at a receiver. Resulting scintillation levels are consistent with standard turbulence models. Increased received intensity and reduced scintillation was observed with larger core fibres and related to aberration-induced focal spot size. Correlation between the received intensity variation and the amplitude variations for individual Zernike modes demonstrates specifically the effect of atmospheric induced beam wander when focusing into a receive fibre. The DMD is thus shown to be able to generate both the necessary frequency content and range of scintillation required for atmospheric emulation.

1. Introduction

Remote optical signalling is one of the oldest forms of communication—dating back to lighthouses, fire beacons etc [1], and free space communications dominated early attempts at long distance communication with light [2]. The development of both the optical fibre and the laser have combined to make high-capacity optical fibre communications the backbone of the modern information age. Indeed, it is so successful that we are in danger of approaching the capacity limit of these fibre devices [3]. To stave off the capacity crunch researchers are seeking new ways to increase capacity, in particular the use of spatial division multiplexing, making use of orthogonal spatial amplitude distributions to carry information in parallel channels [4]. Free space communication offers a number of advantages, including lower installation cost—particularly in harsh environments [5]—and reduced nonlinear effects - enabling good initial signal to noise ratio. Much research attention has now focussed back to free space communication with a view to taking advantage of the same techniques that allow high-capacity data transfer in fibres and using them in an unconfined media such as free space [6–8]. However, transmission through the atmosphere encounters a number of problems not found with fibres that add significant problems when establishing a communications system [2].

1. High precision pointing and alignment is required between transmitter and receiver.
2. An obstruction free path is generally required
3. The effects of diffraction can lead to geometric loss of signal
4. Random refractive index variations in the atmosphere lead to beam wander and breakup.

The first 3 points can be addressed in the engineering of the system. The effects of the atmosphere are random and statistical and have had a significant affect upon system performance. When the atmosphere causes the beam to be steered away from the detector it can result in complete loss of signal—analogous to fading in the RF world. Random phase variations can cause the beam to expand, break up and become discrete reducing the amount of signal collected. This can cause signal loss independent of atmospheric loss arising from scattering and absorption [9]. The phase variations induced across the received wavefront can have a significant effect upon signals relying on coherence detection. For some decades the effects of atmospheric turbulence have been addressed through the use of adaptive optics [10, 11], which typically uses a deformable mirror to counteract the deformations to the optical wavefront. This of course requires the ability to characterise the wavefront 'error', typically done with a Shack Hartmann sensor. Theoretically it has been found that the information is not lost [12] and more recently there is a movement to decompose the atmosphere using mode-to-spatial domain conversion via multiple apertures [13] or a multi plane light converter [14, 15] and to provide correction via digital signal processing. These preliminary results, using spatially diverse approaches (multi-aperture or multi-mode) to mitigate turbulence effects are highly promising, as are parallel attempts to boost capacity with spatial diversity, but require extensive testing to enable reliable network design.

Given the difficulty of conducting atmospheric transmission experiments over distance - finding a suitable testing range, associated cost, total unpredictability of atmospheric conditions, characterisation of those conditions - it is understandable that researchers would seek to find a laboratory-based emulation of atmospheric effects. Approaches have included manipulation of the phase wavefronts using spinning phase plates [16], spatial light modulators [17–22] using liquid crystal(LC-SLM) based devices to produce spatially controlled phase variations, near index-matched optical simulators [23] or the fabrication of elaborate atmospheric emulation chambers [24].

In this work we investigate the use of a binary amplitude spatial light modulator, the digital micromirror device (DMD) [21, 25], as a method of atmospheric turbulence emulation. Why use a binary amplitude modulator rather than a phase modulator which might seem intuitively better suited to phase front control? The principal advantages of the DMD are speed and versatility. The device is an array of tilting micromirrors (typically 10 μm dimensions) which 'flip' between on($+12^{\circ}$) and off (-12°) states at rates in excess of 10 kHz. LC-SLMs have frame rates of around 100 Hz. Atmospheric scintillation effects are known to extend up to around 1 kHz and may typically be several hundred Hz, the LC-SLM cannot fully represent the scale of atmospheric effects, whilst fixed phase plates and atmospheric chambers offer limited flexibility. The DMD as a mature commercial technology can be lower cost than the LC-SLM, operates with wider spectral bandwidth and has higher power handling capacity. The DMD however suffers from poor efficiency, not least due to typically 50% of the mirrors being in the 'off' state and redirecting light out of the system, plus effects of diffraction that arise from the 2D array. Efficiencies may then only be a few percent [25, 26]. A previous example of using a DMD to produce atmospheric type distortions used the DMD to generate static aberrations which are then corrected with an adaptive optics system [27], but no temporal 'scintillation' was presented. In this work we don't just generate turbulent wavefronts we make use of them to explore the effect of fibre core size at the receiver as this has a critical affect on system alignment. We can see which contributions are significant at different levels of turbulence. Along the way we discover key effects that influence the accuracy and efficacy of the technique - such as artificial intensity fluctuations with weak aberrations, the need to separate the diffracted wavefront from undiffracted components using a tilt offset and a sensitivity to scaling between lab scales and real-world scales. Such knowledge and understanding is essential for the researcher wishing to implement the DMD as an atmospheric emulator for free space optical communications.

We anticipate that the use of the DMD to emulate an atmosphere will help pre-empt system design issues, verify DSP methods and inform network design. High switching speeds will enable accurate channel emulation for high turbulence scenarios, whilst programmable turbulence will enable multicanonical Monte Carlo methods to be applied [28], greatly increasing the efficiency of atmospheric conditions liable to induce outage events.

2. Method

The statistical behaviour of light transmitted through the atmosphere was considered using a dimensional analysis approach by Kolmogorov [29] and this forms the standard approach to understanding atmospheric behaviour. The atmosphere is considered to be composed of a collection of cells with a statistical variation in refractive index. The cell size is considered to have an inner and an outer scale. A parameter called the refractive index structure constant (C_n^2) is used to indicate the strength of atmospheric turbulence effects with $C_n^2 = 10^{-17}$ $\mathrm{m}^{-2/3}$ in weak turbulence conditions (good seeing) and $C_n^2 = 10^{-13}$ $\mathrm{m}^{-2/3}$ representing strong turbulence conditions (poor seeing). The Fried parameter (r_0) is the lateral coherence length of the atmosphere and for a

Table 1. Zernike modes in their Cartesian form and their associated optical aberrations, V means vertical, H means Horizontal.

j	Zernike term	Cartesian Form	Name
1	Z_1	1	Piston
2	Z_2	x	Tip
3	Z_3	y	Tilt
4	Z_4	$-1 + 2x^2 + 2y^2$	Defocus
5	Z_5	2xy	V Astigmatism
6	Z_6	$-x^2 + y^2$	H Astigmatism
7	Z_7	$-2x + 3x^3 + 3xy^2$	V Coma
8	Z_8	$-2y + 3y^3 + 3x^2y$	H Coma
9	Z_9	$-x^3 + 3xy^2$	V Trefoil
10	Z_{10}	$y^3 - 3x^2y$	H Trefoil
11	Z_{11}	$1\text{-}6x^2 - 6y^2 + 6x^4 + 6y^4 + 12x^2y^2$	Spherical aberration
12	Z_{12}	$-6xy + 8x^3y + 8xy^3$	V Secondary astigmatism
13	Z_{13}	$3x^2 - 3y^2 - 4x^4 + 4y^4$	H Secondary astigmatism
14	Z_{14}	$-4x^3y + 4xy^3$	V Quadrafoil
15	Z_{15}	$x^4 - 6x^2y^2 + y^4$	H Quadrafoil

plane wave traversing a horizontal path is given by.

$$r_0 = 1.68(C_n^2 L\, k^2)^{-\frac{3}{5}} \tag{1}$$

Where L is the path length and $k = 2\pi/\lambda$ where λ is the wavelength. The Fried parameter limits an imaging system's resolution and represents the effective maximum size limit for an aperture [30].

The shape of a beam in free space may be expanded in any number of modal bases. However, having passed through atmosphere it is most conveniently expressed as a collection of orthogonal modes—Zernike modes (ZM) based on Zernike polynomials. These modes relate to well known fundamental optical aberrations (defocus, coma, astigmatism etc) and hence they are convenient to use in free space. The Zernike modes are usually given in a polar notation [31] however when using a 2D array it is more convenient to use the Cartesian form, shown in table 1, where the x and y values relate to the pixel coordinates.

The optical wavefront can be represented as a sum of these modes:

$$W(x, y) = \sum_{i=1}^{m} a_i Z_i \tag{2}$$

Where the parameter a_i is the amplitude of the mode.

There is often a misunderstanding about how a binary device can control phase, particularly in comparison to a LC-SLM which has fractional phase control of individual pixels. It is easy to conceive of the LC-SLM manipulating the local phase of a wavefront. The DMD creates a distorted wavefront as a result of diffraction. The diffracted wavefront is being distorted by an amount determined by the amplitude of the mode pattern written across the device. The amount of distortion can be fractions of a wavelength because it happens over an extended area. It is important to think about the mode pattern not the individual pixel phase. The DMD is also a 2D blazed diffraction grating that produces a 2D set of diffraction orders close to the blaze direction. The patterns written to the DMD produce diffracted wavefronts replicated at each diffraction order.

Creating DMD binary patterns from the required wavefront phase values is the same process as used with Fresnel Zone plates(FZP) [26] (which is actually just the defocus term Z_4). The FZP is a set of concentric rings that alternate between transparent and opaque and essentially filter light based on phase polarity such that only one polarity of light interferes constructively at the desired focal point. This is an entirely diffractive process that produces a distorted wavefront with a quadratic curvature and hence a focus is produced. This works in the $+24°$ blaze direction where constructive interference occurs at multiple integer wavelengths of a diffraction order. Thus for our required wavefront across the DMD, constructed from the controlled amplitudes of ZMs, we select (i.e. reflect in the 'on' direction) phase values of one polarity. More precise phase selection using so-called superpixels is possible but with much reduced efficiency [32]. Once the wavefront is composed and converted to a wavelength (λ) dependent phase value, a binary pixel value $D(x, y)$ is selected:

$$D(x, y) = \begin{cases} 0, \sin(\frac{2\pi}{\lambda} W(x, y)) < 0 \\ 1, \sin(\frac{2\pi}{\lambda} W(x, y)) \geqslant 0 \end{cases} \tag{3}$$

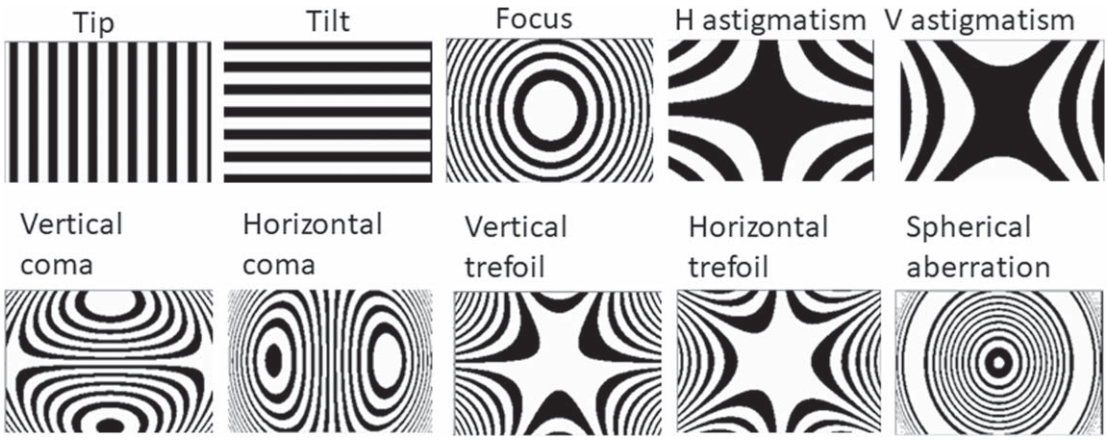

Figure 1. Example Zernike mode patterns for the first 10 modes and their corresponding primary aberrations as represented on a DMD.

Table 2. The error distribution size for specific Zernike modes.

Zernike Mode	Zernike Kolmogorov residual error
Tip	$\Delta_1 = 1.0299(D/r_0)^{5/3}$
Tilt	$\Delta_2 = 0.5820(D/r_0)^{5/3}$
Focus	$\Delta_3 = 0.1340(D/r_0)^{5/3}$
Astigmatism X	$\Delta_4 = 0.111(D/r_0)^{5/3}$
Astigmatism Y	$\Delta_5 = 0.0880(D/r_0)^{5/3}$
Coma X	$\Delta_6 = 0.0648(D/r_0)^{5/3}$
Coma Y	$\Delta_7 = 0.0587(D/r_0)^{5/3}$
Trefoil X	$\Delta_8 = 0.0525(D/r_0)^{5/3}$
Trefoil Y	$\Delta_9 = 0.0463(D/r_0)^{5/3}$
Spherical aberration	$\Delta_{10} = 0.0401(D/r_0)^{5/3}$
Secondary Astigmatism X	$\Delta_{11} = 0.0377(D/r_0)^{5/3}$
Secondary Astigmatism Y	$\Delta_{12} = 0.0352(D/r_0)^{5/3}$
Higher Orders (j > 12)	$\Delta_{13} = 0.2944j^{\sqrt{3/2}}(D/r_0)^{5/3}$

Figure 1 shows example binary patterns for the first 10 primary Zernike modes (excluding piston) and their corresponding primary aberration names obtained by calculating the spatial phase value and then thresholding based on polarity, as represented in equation (3).

The pattern written to the DMD is a digital hologram and can be used to generate any required wavefront [25].

The relationship between the statistical variances of the amplitudes of ZMs and the Fried parameter is well known [33]. Previous authors have used this relationship to generate random amplitude values drawn from statistical distributions with the correct variances. The relations are in table 2 where D is the receiving aperture diameter and r_0 is the Fried parameter [18]. These values show that tip and tilt have the largest amplitudes which relates to a beam wandering up/down and left/right. This has a significant effect on alignment between source and detector - a factor that is particularly significant when focussing into an optical fibre at the receiver.

The orthogonality of the ZMs, in the conventional definition, only holds for circular apertures. The DMD has a rectangular aperture and we could use a set of ZMs with rectangular orthogonality as given in [31]. However, a circular geometry matches the conventional beam shape and to account for this we write an opaque aperture to the DMD with a diameter equal to the smallest dimension of the DMD and use the circular ZMs, which helps improve image quality when the wavefront is focussed.

In order to emulate an atmosphere, for each ZM, Zi, a set of amplitude values $a_i(t)$ are chosen at random from a zero mean Gaussian distribution with a width given by the values presented in table 2. These are used to form a sequence of ZM sets representing a particular instance of a random temporal evolution of the wavefront. The values of D and r_0 are determined by the system and the amount of atmospheric turbulence required in the emulation respectively. A spline fit with a chosen number of intermediate points (usually 10) is then used to produce intermediate points $(a_i(t'))$ ensuring a smooth transition [18]. At each spline point the disturbed wavefront is calculated across the DMD plane.

$$W(x, y, t') = \sum_{i=1}^{m} a_i(t')Z_i \tag{4}$$

The DMD is also itself a source of aberration which will reduce the efficiency with which signals can be collected. The inherent aberrations of the device can be compensated for by the device itself which is a spatial light modulator. This requires a separate procedure to characterise the DMD [34] which is outlined here but will be given in more detail elsewhere. By illuminating the DMD with a plane wavefront and writing suitable ZM patterns (essentially a FZP) to the device, the DMD can be used to focus its reflected light onto a camera sensor. This is done in the visible where cameras are readily available. By scanning amplitude values for the ZMs and measuring the focal spot quality on the camera, optimum values for the ZM amplitudes can be found. The focal spot quality metric in its simplest form is the maximum intensity achieved at the focus, but must also account for the shape of the spot being as circular as possible. These resultant ZM amplitudes represent the inverse values of the device aberrations where the device is correcting itself. If we remove the focus value (which is creating the focus onto the camera) and remove the astigmatism values (which result from off axis reflection) then the remaining values represent the inherent aberrations of the device and can be used as a device profile and this can be added to the wavefront. The amplitude values of ZMs represent an equivalent physical distortion and must be scaled for wavelength changes to represent phase variation.

The wavefront sequence is then:

$$W(x, y, t') = \sum_{i=1}^{m} [a_i(t') + p_i + q_i]Z_i \tag{5}$$

Where p_i are the set of profile amplitudes, scaled according to wavelength and q_i are optional constants that are used for beam control.

3. System setup

The intended experiment here is to reflect a beam from the DMD, distorting the wavefront according to a series of aberrating patterns. The light is then collected and focused into a fibre, examining the effect upon the collected intensity caused by the simulated atmospheric turbulence pattern written to the DMD.

The DMD system had 1280 $\times$ 800 mirror pixels and each mirror was square with 10.8 μm dimension. The system had a near IR antireflection coating and a maximum switching speed of 10,752 Hz. The output from a narrow linewidth laser (Koheras) was expanded to overfill the size of the DMD circular pattern. The DMD operates as a 2D blazed grating so the collecting fibre is aligned with direction of the strongest order closest to the angle of reflection. A schematic diagram of the system is shown in figure 2. A 3x beam expander is used in reverse to reduce the size of the beam, ensuring the beam entering the collimator does not exceed the numerical aperture of the fibre. The captured light is then detected by an InGaAs photodiode, amplified and measured with a data acquisition unit and viewed on a computer.

3.1. Refinements

In testing it was noticed that some small changes in ZM parameter amplitudes resulted in significant changes in detected intensity. This change was correlated with the shape and polarity of the pattern being projected—see figure 3. When strong levels of aberration are present—such as when focusing with a Fresnel zone plate—the number of black and white pixels are the same across the whole image with 50% of each. However, when the aberrations are weaker this equality need not be maintained and having more white than black pixels results in a higher intensity being directed towards the fibre. This problem can be exacerbated when using a Gaussian intensity profile laser beam as more weight is given to the central pixels. To rectify this issue the following normalisation process was used: For each frame the white to black pixel ratio (R) was measured. If there were more black pixels (R $<$ 0.5) then the inverse pattern was produced. The number of white pixels that need to be removed is ((R-0.5)/2 and this number of white pixels selected at random can be removed to bring the ratio to 0.5.

At the end of each frame the DMD system resets by switching all mirrors to the 'off' position. This results in a regular loss of signal, in the present case for a time of 93 μs. All data presented here shows the received intensity modulations with these signal drops removed but these 'dark periods' must be accounted for within the context of the application of the system.

The intended emulation utilises a receive aperture D, (and path length L) that are much larger than the actual aperture of the DMD (d) in the lab. Thus we must scale the effects accordingly to account for system constraints. The tilt jitter variance arising from the two axis Zernike tip-tilt can be represented by [30]:

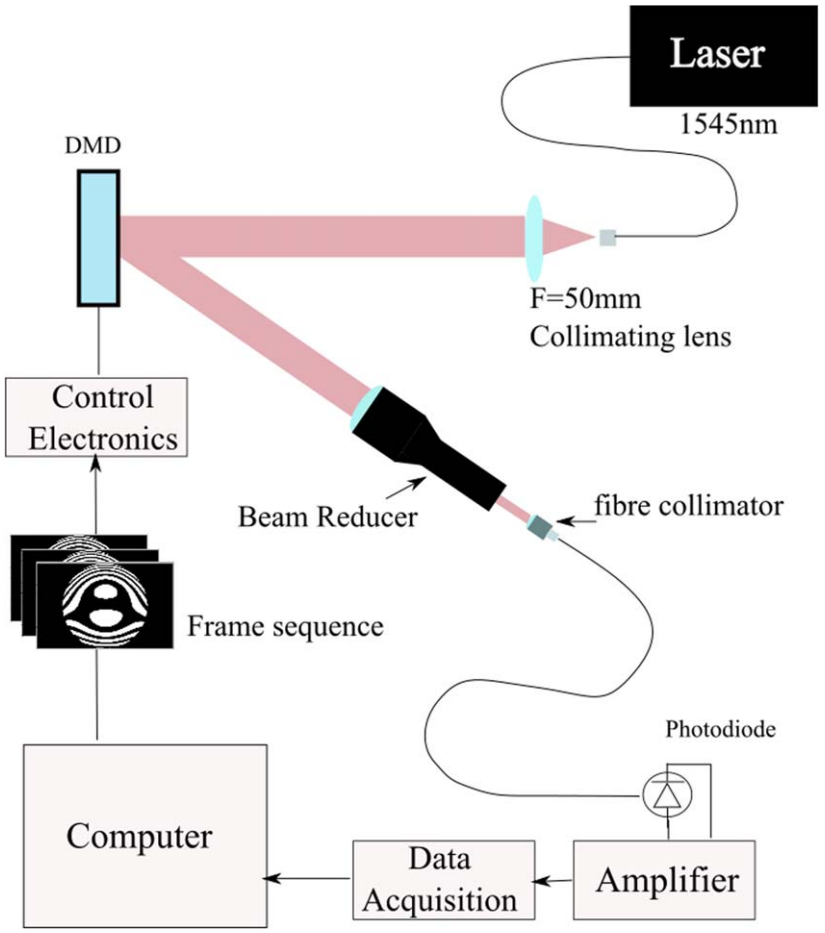

Figure 2. A schematic diagram of the DMD based atmospheric emulation system setup with the beam shown originating from the micromirrors in the 'on' state tilted at 12°.

$$T_z^2 = 0.36\left(\frac{D}{r_0}\right)^{5/3}\left(\frac{\lambda}{D}\right)^2 \tag{6}$$

The tilt phase variance is defined as the tilt variance divided by the factor $(4/kD)^2$

$$\sigma_T^2 = 0.90\left(\frac{D}{r_0}\right)^{5/3} \tag{7}$$

i.e. the atmospheric induced phase variance for an aperture D, which is now presented across the smaller aperture d. Thus the ZM phase variances given in table 2 must all be scaled by a factor

$$S = \left(\frac{d}{D}\right)^{5/3} \tag{8}$$

The control of the wavefront is achieved through diffraction - choosing the appropriate spatial pattern upon the DMD. The DMD is a 2-dimensional blazed diffraction grating which produces 'grating orders' (that are independent of the pattern) through the combined effect of a 2D array (a 2D comb) and the angled mirrors. Detectors must be placed at an angle to the DMD axis matching the constructive order position in the 'on' position. In the case of a wavelength around 1.5 μm this corresponds to an order number (n) of 7 at close to double the mirror tilt angle. In addition to this there are local 'pattern orders' which are the 2D Fraunhofer diffraction patterns of the pattern written to the DMD which are replicated at each grating order. These pattern orders also have order numbers ($m = 0, \pm 1\ldots$) and can produce multiple diffraction patterns. Of particular interest here is the zeroth order which is an undiffracted beam. This behaves as a background level upon which the diffracted beams will sit. In the context of atmospheric emulation this is undesirable as the zeroth order beam acts as a background to the diffracted beams and will obscure the emulated turbulence effects. The orders can be separated through the controlled addition of tip and tilt to the ZM constructed wavefront. This is conventionally done with a spatial filter, selecting the first order diffraction beam, but using the fibre as the collection aperture is equivalent. This was tested with the use of a static tip/tilt pattern written to the DMD and the beam steered to a position where only the wanted first order beam is directed into the collecting fibre. This reduced the intensity in

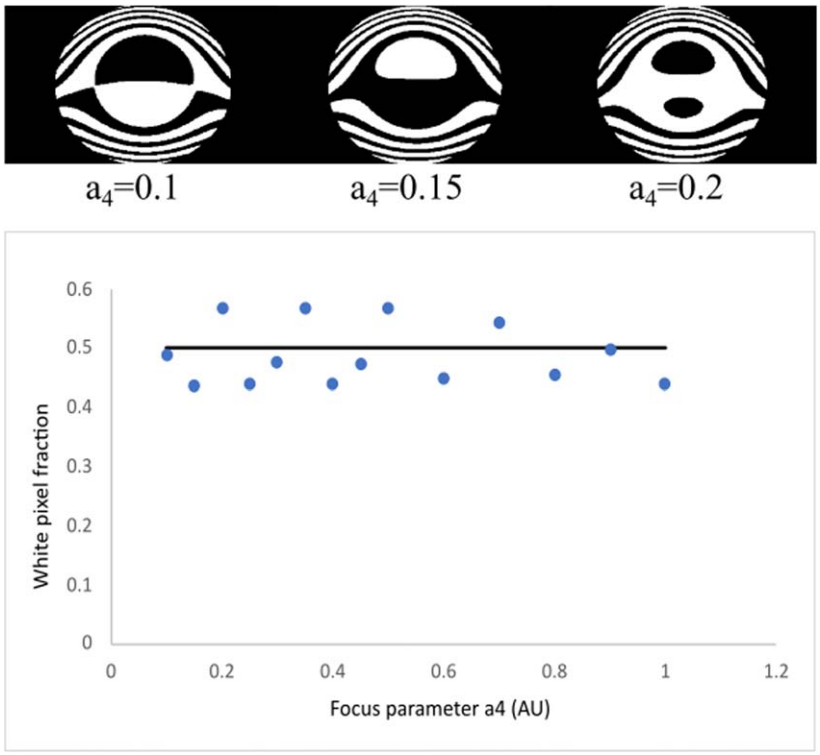

Figure 3. This figure shows how small changes in parameters can lead to large change in reflected intensity. The patterns at the top contain small amounts of focus, astigmatism and spherical aberration. Only focus is changed with the amplitude showed below the plot. The lower plot is the ratio of white to black pixels for different values of the focus amplitude.

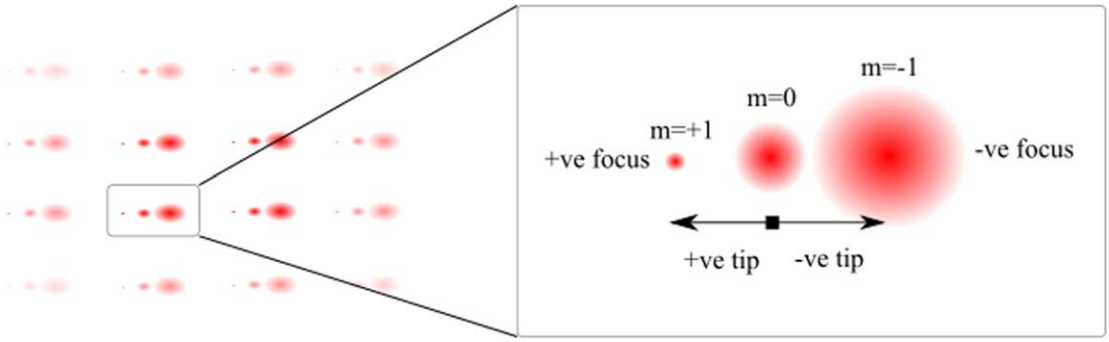

Figure 4. A diagram representing the diffraction orders from a DMD with a focus and tilt pattern applied. This shows the grating orders and the pattern orders with order separation due to tilt and focusing dependent on order polarity.

the zeroth order by 50% and the intensity in the first order to 20% of the unseparated level. With this arrangement the necessary tip and tilt amplitudes can be added as offset values (q values in equation (5)) to the statistical tip and tilt values used to represent turbulence. An alternative possibility is to add an offset value to the focus term and realign the system focus away from the standard focus position, but this was found to be a less flexible approach. It is worth stating for completeness that the sign of the pattern order affects the nature of the focus in the orders, such that the $m = +1$ order adds positive focus, whilst the $m = -1$ order defocuses by the same amount [35]. This can be seen in figure 4 which is a representation of DMD diffraction and is the result of a focus and tilt pattern. The separation of zero and first order as a result of the application of tilt are shown in the magnified detail.

Sequences of frames were produced where the amount of atmospheric turbulence was selected by choosing a value for C_n^2 as well as a receiver aperture diameter and the distance from transmitter to receiver. Then random values for scaled ZM amplitudes were selected as described above and then the tip and tilt offsets were added. Sequences were typically 400 frames long and all frames were uploaded to the DMD control board. The timescale for the sequence could be varied by controlling the time per frame.

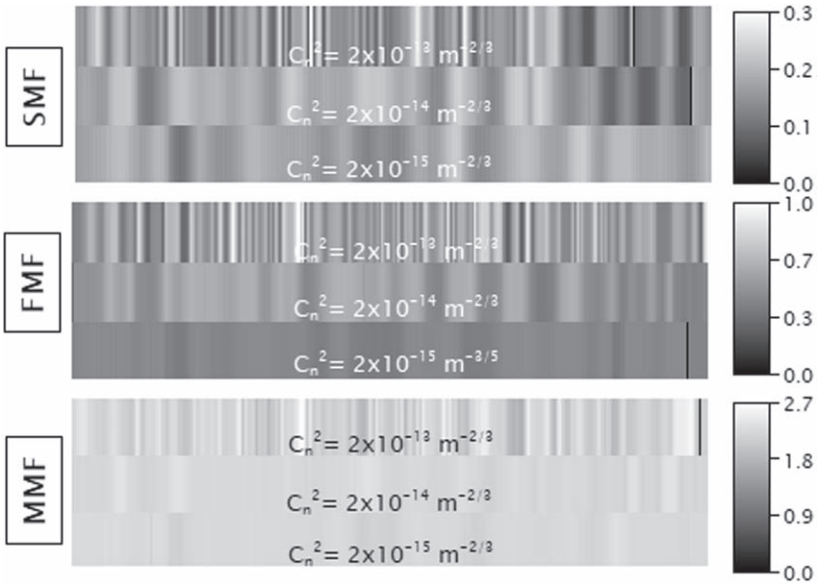

Figure 5. Measured intensity variations for sequences with increasing values of C_n^2 captured by a SMF (top set of bars), FMF (centre set) and MMF (lower set). Signal intensity is represented as a grey scale consistent for each fibre type. The horizontal scale matches with frames of the sequence applied. Higher C_n^2 values show a larger amount of intensity variation and MMF intensities are higher than SMF and FMF.

4. Results

In order to emulate a demanding communication link, when calculating the amount of scintillation to apply, the model aperture size was chosen to be $D = 10$ cm and the model range between transmitter and receiver set to $L = 1$ km, with 22 Zernike modes being used. The values of D and L were chosen to be representative of a real world FSO comms scenario with achievable optics that give efficient collection. In the laboratory emulation of this model the distance between DMD and collecting fibre was around 0.5 m.

Different sequences of 400 frames were produced for moderate to strong turbulence values with C_n^2 values of $2 \times 10^{-15}\mathrm{m}^{-2/3}$ to $2 \times 10^{-13}\mathrm{m}^{-2/3}$. The measured intensity variations from these scintillation sequences are shown in figure 5. This shows a progressive increase in the frequency of variation as the C_n^2 level increases. For each scintillation sequence the received intensity was recorded for both a single mode fibre (SMF), a few mode fibre (FMF) and also a multi-mode fibre (MMF). This allows direct comparison of the effect of fibre mode area on the received power under the exact same aberrating conditions.

The wavefront aberrations cause a broadening of the focal spot beyond the size of the fibre core, reducing the intensity in the smaller core fibre and reducing the scintillation level in the larger core. The wavefront variance σ^2 is related to the ZM amplitudes [36]:

$$\sigma^2 = \frac{{a_3}^2}{5} + \frac{{a_{10}}^2}{9} + \frac{1}{2}\left[\frac{{a_1}^2}{2} + \frac{{a_2}^2}{2} + \frac{{a_4}^2}{5} + \frac{{a_5}^2}{5} + \frac{{a_6}^2}{5} + \frac{{a_7}^2}{6} + \frac{{a_8}^2}{6} + \frac{{a_9}^2}{5}\right] \tag{9}$$

The wavefront variance is in waves and the amplitudes are normalized to the values at the maximum radius giving 1 wavelength of aberration. The Strehl ratio, the spot size in relation to diffraction limited spot size, can be related to the wavefront variance via:

$$Strehl = e^{-2\pi\sigma^2} \tag{10}$$

The expected spot size can then be estimated from

$$x = \frac{1.22\,\lambda\, f}{d_{beam}} M * Strehl \tag{11}$$

Where f is the focal length of the collimator (11.3 mm), d_{beam} is the input beam diameter (3 mm) and M is an angular magnification factor (3) resulting from the use of a beam reducer. Using the ZM amplitudes for the lowest level of scintillation the average focal spot size is around 15.5 μm, larger than the core diameter of the SMF and FMF. The mean captured intensity rises as the size of the capturing fibre core increases, due to capturing

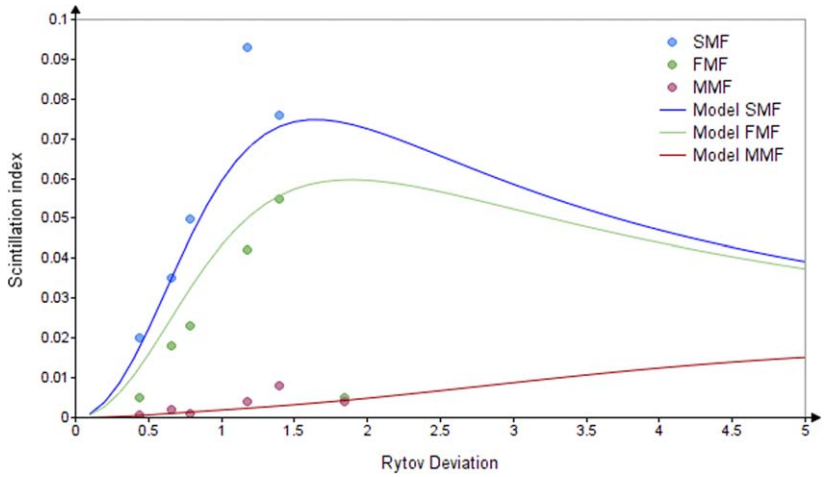

Figure 6. Measured and modelled scintillation index values for single, few and multi mode fibres for various levels of atmospheric turbulence. The plot is presented in terms of the Rytov variance parameter for comparison with conventional models for a plane wave.

more of the aberrated focal spot, although less than would be expected [37] from the fibre core areas. This is most likely from some residual loss due to exceeding the NA of the fibres.

In order to verify the scale of the emulated scintillation for the chosen C_n^2 parameters we determine the scintillation index, given by:

$$\sigma_I^2 = \frac{\langle I^2 \rangle}{\langle I \rangle^2} - 1 \tag{12}$$

Where I is the intensity and the brackets represent the average value. Scintillation index values for all the sequences and for all the receiving fibres are shown in figure 6 along with theoretical values for the scintillation index for a plane wave source (see appendix) in terms of the chosen values of C_n^2. The theoretical scintillation index values are for the chosen scenario of transmission distance of 1 km and receive aperture of 10 cm. The plot shows scintillation index in terms of the Rytov parameter

$$\sigma_R^2 = 1.23 C_n^2 k^{7/6} L^{11/6} \tag{13}$$

Assuming the MMF captures all of the light focused from the collection aperture, the SMF and FMF models use a reduced aperture diameter scaled by the ratio of the fibre core size to the MMF core size. The effect of the beam reducer must also be included as this increases the effective amount of scintillation with increased angular magnification. As should be expected from the beam spot size calculations, the smaller fibre cores show increased levels of scintillation corresponding to a smaller effective aperture size. The scintillation levels are of the right order but appear to reduce faster than the model, which suggests fine tuning of the scaling factor is required to relate the desired C_n^2 value to the ZM amplitudes. We can see from figure 6 that although the C_n^2 represent a strong turbulent atmosphere, the Rytov variance values for this scenario represent weak fluctuations as they are found on the left hand side of the model curve. This is due to the modest range (L) and relatively large aperture, which are the specific circumstance that we wish to investigate. This tells us 2 things of value. Firstly that the DMD induced scintillation can be made at a controllable and appropriate level with careful calibration of the ZM amplitudes. Secondly the chosen scenario of a 1 km path and a 10 cm aperture is both workable in practice and can be emulated in a lab.

The ZM amplitudes for each frame in each sequence were recorded and are represented in figure 7.

The upper plot shows the evolution of the first 12 mode amplitudes with the strongest variations in the lowest order modes—tip and tilt. The received intensity variation for this set of amplitudes is shown in the lower plot. Each ZM amplitude set ($a_i(t')$ in equation (5)) can then be correlated with the recorded intensity for that sequence. The correlations for each ZM evolution with the received intensity variation are shown in figure 8 for SMF, FMF and MMF for 3 values of C_n^2. Given that the intensity variation is the net result of all ZM variations we would not expect high correlation values for any single mode. However it is clear that at weaker C_n^2 values the strongest correlations are with the tip and tilt parameters. This is an anti-correlation as would be expected as either polarity of displacement moves the focus away from the best focus and reduces the received intensity. At higher C_n^2 of 1×10^{-13} m$^{-2/3}$ the correlation is essentially broken. Caution must be used in interpreting these correlations as they express the correlations viewed *in this system* and may be relevant by extension to a similar FSO system undergoing atmospheric scintillation.

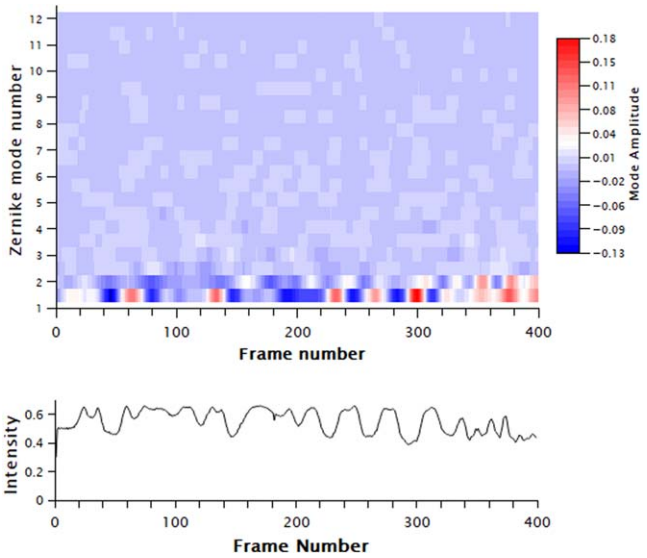

Figure 7. Zernike mode amplitudes for each frame in the $C_n^2 = 1 \times 10^{-14}\,m^{2/3}$ sequence. The upper plot shows the temporal sequence for the first 12 Zernike mode amplitudes, as used for each frame. The amplitude variation for higher order modes decrease as per table 2 with tip and tilt being the largest. The lower plot is the measured intensity level captured by a FMF for the same frame sequence.

5. Discussion

The development of modelling of atmospheric turbulence effects upon optical beams has traditionally taken the approach of considering intensity fluctautions within a given aperture - a bucket detector. When that aperture is a lens that is focussing into a fibre there are effects upon the measured scintillation characteristics that effectively change the aperture size in nonlinear ways. These result from the small size and modal characteristics of the receiving fibre. For example focussing into a fibre is sensitive to the lens to fibre distance where matching focal spot size to core size is required. Changes to the input beam focus will defocus the beam onto the fibre and reduce the captured intensity as the square of that defocus. We would therefore expect the measured intensity variations for a SMF to be modified in comparison to those actually introduced by atmospheric turbulence (or an emulator). The modulation transfer function of the collection system must be included. This is is particularly relevant when considering the use of spatial division multiplexing. Higher order ZMs induced by atmospheic turbulence can lead to increased loss by the numerical aperture (modal loss) of fibre used for collection as well as modal cross talk when combined with tip and tilt displacement within multi-mode fibres. The oberved correlation between individual ZMs and the received intensity variations should prove valuable in characterising modal cross talk. It will help in targetting which modes are most severely affected or resistant in a SDM FSO system.

6. Conclusion

This work has sought to use the spatial light modulation capabilities of a DMD micro-mirror array to emulate the effects of turbulence in the atmosphere for use with an FSO communication system. The high-speed capabilities of this SLM in comparison to liquid crystal based SLMs or video rate systems are a clear benefit to using the DMD which would be easily capable of reproducing effects in excess of 1 kHz which would be present in high levels of turbulence if required. Sequences of turbulence aberrations constructed from Zernike modes with various levels of C_n^2 and passed to the DMD at rates of 400 Hz but this can be easily scaled to different rates.

In addressing the suitability of the DMD for use as an atmospheric emulator the major issues are the low efficiency, the need for normalising the intensity and the dark time at the end of each frame. For use in FSO comms the most significant of these is the dark time. The dark time is dependent upon the model of DMD system and this case was 93 μS, which is short on the timescale of the atmosphere but very long on the time scale of communications signals. Thus, synchronisation between the data packet structure and the frame transitions of the DMD would be required to ensure effective use. The dark time is a feature of the particular system being used, allowing frame set up and synchronisation, and can in principle be reduced significantly. Future systems may not suffer from this restriction. Whilst phase based SLMs are more efficient in their utilisation of intensity,

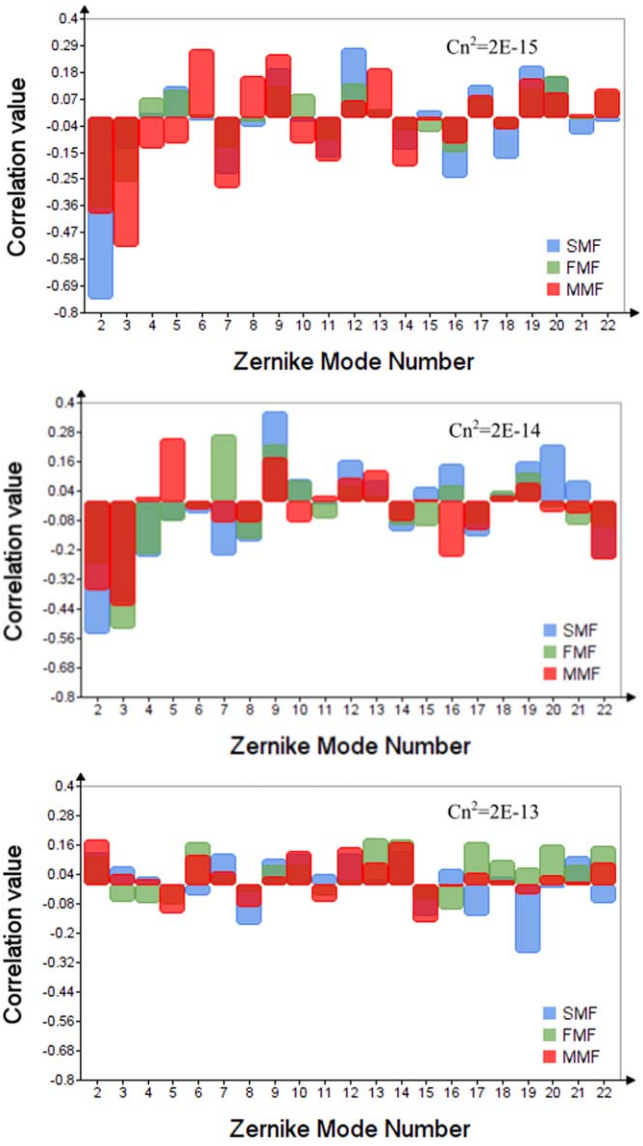

Figure 8. Correlation coefficients for each ZM amplitude set with the received signal for each fibre. The value of Cn2 for the sequence used is given on each plot.

they will also suffer with settling time as their pixels transition between states but clearly on a larger time scale than the DMD.

The results from using different sizes of fibre show that using larger area fibres reduced the level of scintillation observed without changing the physical aperture size of the collecting lens, and also collected more of the incoming light. In systems that transition from free space to fibre the use of SMFs is desired for maintaining integrity along the fibre system but is clearly a source of significant loss to the system as a whole. With SDM larger area fibres are necessary so they will be more efficient. The challenge is then to separate the spatial modes and compensate for mixing and mode dependent loss. As this must be done anyway it makes sense to move straight to using MMFs to maximise efficiency and place effort into larger scale mode separation.

The current system is useful in demonstrating the principle of using ZMs on a DMD and how that interacts with a system. In particular being able to correlate the individual ZMs in a sequence with the output intensity variations can provide useful information about how and where the received power is being distributed and should help with understanding the scale and extent of modal cross talk for SDM systems. We have shown that the DMD is capable of implementing a wide range of scintillation levels but further work is required to characterise and calibrate the precise relationship between ZM amplitudes and resulting scintillation.

In the present case, whilst the timescale can be varied, each mode was varying along the same timescale. This is clearly unphysical and higher order modes should be responsible for the higher frequency components in the intensity fluctuations. This should be a focus of future work. Further work is required to understand the transfer

connection between the higher order ZMs and the Laguerre–Gaussian modes of the fibre. Correlating the ZM amplitudes with separated modal intensities post receive fibre will help this.

Data availability statement

The data that support the findings of this study are available upon reasonable request from the authors.

Funding

The authors wish to acknowledge the financial support of the EPSRC under grant number EP/T009047/1. Yiming Li is has received funding from the European Union's Horizon 2020 research and innovation programme under the Marie Skłodowska-Curie grant agreement No 713694.

Appendix

Under weak fluctuations the scintillation index for an infinite plane wave propagating along a horizontal path leads to the Rytov variance

$$\sigma_R^2 = \sigma_{I,pl}^2 = 1.23 C_n^2 k^{7/6} L^{11/6} \tag{A1}$$

All relationships are taken from [30]

The effect of collecting with an aperture is to average and reduce the fluctuations relative to a point detector. Under weak-to-strong intensity fluctuations the scintillation index for a receiver aperture size D is

$$\sigma_{I,pl}^2(D) = \exp\left[\frac{0.49\,\sigma_R^2}{(1+0.65d^2+1.11\sigma_R^{\frac{12}{5}})^{7/6}} + \frac{0.51\,\sigma_R^2\,(1+0.69\sigma_R^{\frac{12}{5}})^{-5/6}}{(1+0.90d^2+0.62\,d^2\,\sigma_R^{\frac{12}{5}})^{5/6}}\right] - 1 \tag{A2}$$

Where

$$d = \sqrt{\frac{kD^2}{4L}}$$

For a spherical wave the scintillation index reduced due to aperture averaging is:

$$\sigma_{I,sph}^2(D) = \exp\left[\frac{0.49\,\beta_0^2}{(1+0.18d^2+0.56\,\beta_0^{\frac{12}{5}})^{7/6}} + \frac{0.51\,\beta_0^2\,(1+0.69\sigma_R^{\frac{12}{5}})^{-5/6}}{(1+0.90d^2+0.62\,d^2\,\beta_0^{\frac{12}{5}})^{5/6}}\right] - 1 \tag{A3}$$

Where $\beta_0^2 = 0.5 \quad C_n^2 \quad k^{7/6} \quad L^{11/6}$

Gaussian beams produce aperture averaged scintillation indices that lie between spherical and plane waves.

ORCID iDs

David M Benton https://orcid.org/0000-0003-0663-1404

References

[1] Agrawal G P 2016 Optical communication: its history and recent progress *Optics in Our Time* (Cham: Springer) Ch 8 pp177–99
[2] Goodwin F E, Nussmeier T A and Zavin J E 1973 A 10.6 μm terrestrial communication link *International Telemetering Conference Proceedings* (http://hdl.handle.net/10150/604615)
[3] Ellis A D, Suibhne N M, Saad D and Payne D N 2016 Communication networks beyond the capacity crunch *Phil. Trans. R. Soc. A* **374** 20150191
[4] Richardson D, Fini J and Nelson L 2013 Space-division multiplexing in optical fibres *Nature Photon* **7** 354–62
[5] Lavery M P J *et al* 2018 Tackling Africa's digital divide *Nature Photonics* **12** 249–52
[6] Belmonte A and Kahn J M 2009 Capacity of coherent free-space optical links using diversity-combining techniques *Opt. Express* **17.15** 12601–11
[7] Abadi M M, Cox M A, Alsaigh R E, Viola S, Forbes A and Lavery M P J 2019 A space division multiplexed free-space-optical communication system that can auto-locate and fully self align with a remote transceiver *Sci. Rep.* **9** 1–8
[8] Willner A E *et al* 2015 Optical communications using orbital angular momentum beams *Adv. Opt. Photon.* **7** 66–106
[9] Ata Y and Korotkova O 2022 Integrating optical turbulence into Beer's law *Laser Phys. Lett.* **19** 046201
[10] Wang Y, Xu H, Li D, Wang R, Jin C, Yin X, Gao S, Mu Q, Xuan L and Cao Z 2018 Performance analysis of an adaptive optics system for free-space optics communication through atmospheric turbulence *Sci. Rep.* **8** 1–11
[11] Liu C, Chen M, Chen S and Xian H 2016 Adaptive optics for the free-space coherent optical communications *Opt. Commun.* **361** 21–4

[12] Hellman M E, Flower R A, Levitt B K and Kennedy R S 1970 Processing and Transmission of Information *Research Laboratory of Electronics (RLE) at the Massachusetts Institute of Technology (MIT)* (https://dspace.mit.edu/handle/1721.1/55706)
[13] Geisler D J, Yarnall T M, Stevens M L, Schieler C M, Robinson B S and Hamilton S A 2016 Multi-aperture digital coherent combining for free-space optical communication receivers *Opt. Express* **24** 12661–71
[14] Fontaine N K *et al* 2019 Digital turbulence compensation of free space optical link with multimode optical amplifier *IET Conf. Publications, 2019 (CP765), 4–7*
[15] Billault V *et al* 2021 Free space optical communication receiver based on a spatial demultiplexer and a photonic integrated coherent combining circuit *Opt. Express* **29** 33134
[16] Rhoadarmer T A and Angel J R P 2001 Low-cost, broadband static phase plate for generating atmospheric like. turbulence *Appl. Opt.* **40.18** 2946–55
[17] Rickenstorff C, Rodrigo J A and Alieva T 2016 Programmable simulator for beam propagation in turbulent atmosphere *Opt. Express* **24** 10000
[18] Wilcox C C, Santiago F, Martinez T, Andrews J R, Restaino S R, Corley M, Teare S W and Agrawal B N 2010 A method of generating atmospheric turbulence with a liquid crystal spatial light modulator *Advanced Wavefront Control: Methods, Devices, and Applications VIII (7816, p. 78160E). International Society for Optics and Photonics.*
[19] Jolissaint L 2006 Optical turbulence generators for testing astronomical adaptive optics systems: a review and designer guide *Publ. Astron. Soc. Pac.* **118** 1205–24
[20] Burger L, Litvin I A and Forbes A 2008 Simulating atmospheric turbulence using a phase-only spatial light modulator *S. Afr. J. Sci.* **104** 129–34
[21] Wilcox C C and Restaino S R 2009 A new method of generating atmospheric turbulence with a liquid crystal spatial light modulator *New Developments in Liquid Crystals, Book* ed Georgiy V Tkachenko ISBN 978-953-307-015-5, 2009, I-Tech (Vienna, Austria) p 234
[22] Korotkova O and Toselli I 2021 Non-classic atmospheric optical turbulence: review *Appl. Sci.* **11** 1–30
[23] Dixit A, Porwal V, Kumar A and Mishra S K 2020 Systematic characterization of near-index-matched optics based atmospheric turbulence simulator *Mapan - J. Metrol. Soc. India* **35** 221–32
[24] Le-Minh H, Ghassemlooy Z, Ijaz M, Rajbhandari S, Adebanjo O, Ansari S and Leitgeb E 2010 Experimental study of bit error rate of free space optics communications in laboratory-controlled turbulence *2010 IEEE Globecom Workshops* pp 1072–6
[25] Scholes S, Kara R, Pinnell J, Rodríguez-Fajardo V and Forbes A 2019 Structured light with digital micromirror devices: a guide to best practice *Opt. Eng.* **59** 041202
[26] Benton D M 2017 Multiple beam steering using dynamic zone plates on a micro-mirror array *Opt. Eng.* **57** 1–13
[27] Anzuola E and Belmonte A 2016 Generation of atmospheric wavefronts using binary micromirror arrays *Appl. Opt.* **55** 3039
[28] Kamalakis T, Sphicopoulos T, Muhammad S S and Leitgeb E 2006 Estimation of the power scintillation probability density function in free-space optical links by use of multicanonical Monte Carlo sampling *Opt. Lett.* **31.21** 3077–9
[29] Kolmogorov A 1941 The local structure of turbulence in incompressible viscous fluid for very large Reynold's Numbers *Rendus de l'Acad. de Sci de l'URSS* **30** 301–5
[30] Andrews L C 2019 *Field guide to Atmospheric optics* 2nd (Bellingham: SPIE)
[31] Dai G-M and Mahajan V N 2006 Orthonormal polynomials in wavefront analysis: Error analysis *Optics InfoBase Conference Papers* **24** 2994–3016
[32] Goorden S A, Bertolotti J and Mosk A P 2014 Superpixel-based spatial amplitude and phase modulation using a digital micromirror device *Opt. Express* **22** 17999
[33] Noll R J 1976 Zernike polynomials and atmospheric turbulence *J. Opt. Soc. Am.* **66** 207–11
[34] Benton D 2021 Aberration and coherence effects with a micromirror array *Proc. SPIE 11867, Technologies for Optical Countermeasures XVIII and High-Power Lasers: Technology and Systems, Platforms, Effects V* **118670D**
[35] Blanchard P M and Greenaway A H 1999 Simultaneous multiplane imaging with a distorted diffraction grating *Appl. Opt.* **38** 6692–9
[36] Wyant J C and Creath K 1992 Basic wavefront aberration theory for optical metrology *Applied Optics and Optical Engineering* **11** 28–39
[37] Krimmer J, Füllner C, Freude W, Koos C and Randel S 2020 Statistical analysis of free-space-to-fiber coupling under atmospheric turbulence *Photonic Networks and Devices* NeM4B.3, Optical Society of America